

Development of an ultrafast detector and demonstration of its oscillographic application*

Houzhi Cai,¹ Qiuyan Luo,¹ Kaixuan Lin,¹ Dong Wang,¹ Junkun Huang,¹ and Jinyuan Liu^{1,†}

¹Key Laboratory of Optoelectronic Devices and Systems of Ministry of Education and Guangdong Province, College of Physics and Optoelectronic Engineering, Shenzhen University, Shenzhen 518060, China

A dilation X-ray detector (DIXD) based on time dilation and microchannel plate (MCP) gated technology has been reported. The DIXD passes a driving pulse along the transmission photocathode (PC) to obtain a dilated electron signal and finally achieves a high time resolution of 12 ps. Furthermore, the waveform of the PC driving pulse can be obtained using the DIXD, and a DIXD oscillographic function can be obtained. An experiment is presented to demonstrate the DIXD oscilloscope. The waveform of the PC driving pulse from points t_1 to t_2 is achieved by the DIXD. The waveform agrees well with that measured by a high-speed oscilloscope with a difference of less than 6%. The maximum theoretical bandwidth of the DIXD oscilloscope is theoretically studied. The bandwidth is limited by the potential difference between the PC and mesh. When the potential difference is 3.4 kV, the theoretical limiting bandwidth is 1000 GHz. The bandwidth increases with an increase in the potential difference.

Keywords: Inertial confinement fusion, Ultrafast diagnosis, Dilation X-ray detector, X-ray framing camera, Microchannel plate

I. INTRODUCTION

Deuterium and tritium can be used in nuclear fusion to release large amounts of energy. Inertial confinement fusion (ICF) and magnetic confinement fusion (MCF) may be effective methods for achieving nuclear fusion [1–9]. In ICF or MCF experiments, plasma diagnostics technology should be used to obtain data for analyzing the fusion process. Two-dimensional ultrafast X-ray cameras based on gated microchannel plate (MCP) are widely used in ICF experiments to image the implosion shape and measure the peak X-ray emission [3]. Such cameras have been successfully applied in ICF facilities such as SG-III, NIF, and OMEGA over several decades [10–13]. They achieve a high time resolution of 35–100 ps by conveying an ultrashort electrical pulse onto an MCP microstrip transmission line to gate photoelectrons [14–16]. However, for the requirements of current ICF that always step at a higher level, for example, the self-emission process with a 100 ps duration, the time resolution cannot be served. Faster cameras should be developed to diagnose such ultrafast processes [17]. Recently, a camera named the dilation X-ray imager (DIXI) was developed, and its time resolution was improved to greater than 10 ps by using time-dilation technology [18–20]. Prosser first introduced electron beam velocity dispersion in 1976 to improve the electronic detector bandwidth [21–23]. This technology was applied to the DIXI in 2010 by Hilsabeck et al. [18]. The DIXI dilates the electron signal converted from the incoming X-ray signal. Then, the temporally magnified electron signal is sampled by a time-resolved MCP imager to achieve a high time resolution. The electron signal time-dilation unit contains a transmission photocathode (PC), grounded anode mesh, and electron drift tube. A negative high DC voltage plus a dilating pulse are applied to the PC to achieve a time-dependent electric field between the PC and mesh, which results in electron energy dispersion. The photoelectrons born earlier can acquire larger energies than those born later, and they drift faster in the region from the mesh to the MCP. Therefore, the time duration of the electron signal is magnified up to 50 times. Subsequently, the temporally magnified electron signal is sampled by a 200 ps time-resolved MCP imager [20]. The DIXI time resolution is greatly improved because of the temporally magnified electron signal.

In this study, a dilation X-ray detector (DIXD) is developed, the waveform of the driving pulse on the PC is measured using the DIXD, and the oscillographic function of the DIXD is presented. Theoretical analysis and

* Supported by the Program for National Natural Science Foundation of China (NSFC) (11775147); Guangdong Basic and Applied Basic Research Foundation (Nos. 2019A1515011474 and 2019A1515110130); Shenzhen Science and Technology Program (Nos. JCYJ20210324095007020, JCYJ20200109105201936, and JCYJ20190808115605501).

† Corresponding author, ljy@szu.edu.cn

experimental verification are performed to demonstrate the performance of the DIXD oscilloscope. This study provides a novel approach for the development of new high-speed oscilloscopes. The differences between our DIXD and Hilsabeck's DIXI are the electron imaging system and time-resolution measurement method. In the DIXI, an electron imaging system consisting of four solenoid magnet coils is used to image electrons from the PC onto the MCP. Coils with large excitation currents are used to generate a 370 Gauss axial uniform magnetic field, which achieves a spatial resolution of approximately $510\text{ }\mu\text{m}$ for the Au PC with a three-fold image demagnification [20]. However, a large excitation current may generate a considerable amount of Joule heat. Fortunately, the pulsed excitation current can be used to reduce the Joule heat. Engelhorn et al. successfully used a pulse with a duration of $\sim 1\text{--}10\text{ ms}$ and a peak current of $\sim 1\text{ kA}$ to excite magnet coils [17]. In the DIXD, a short magnetic lens with a large aperture was employed, which generated an axisymmetric non-uniform magnetic field. The electrons were imaged from the PC onto the MCP at an image ratio of 1:1. Such a short magnetic lens has been frequently applied in streak cameras and electron microscopy to improve the optical-electronic imaging quality or focusing ability [24–26]. The short magnetic lens was excited by a small current to obtain a high spatial resolution, thereby reducing the Joule heat. Certainly, a short magnetic lens has the disadvantage of non-uniform spatial resolution. The spatial resolution worsens with increasing off-axis distances. Three or more short magnetic lenses should be used to improve the spatial resolution of the PC edge.

Another difference is the time resolution measurement method. In the DIXI, a Mach–Zehnder interferometer is used to measure the time resolution. An ultraviolet (UV) light pulse is passed through a Mach–Zehnder interferometer to output a pair of pulses. Each leg of the interferometer contains an aperture in the shape of an arrow. The arrow aperture in the fixed-length leg of the interferometer is horizontal, whereas that in the variable-length leg is vertical. The two laser pulse outputs from the interferometer are detected by the DIXI, which outputs a horizontal arrow image and a vertical arrow image. The arrival time of the laser pulse which produced the horizontal arrow image is set at the center of the DIXI gating time interval. The optical path length of the vertical-arrow UV pulse is then adjusted. The vertical arrow image appears and then disappears over a $\sim 5\text{ ps}$ temporal adjustment, which demonstrates that the DIXI has a 5 ps time resolution [18]. Six images were used to obtain DIXI time resolution. It has a shot-to-shot timing jitter, such as the PC driving pulse jitter, MCP ultrashort pulse jitter, or laser jitter, which could affect the 1.66 ps optical path time between the two adjacent images. The jitter leads to an unstable optical path time and might cause measurement errors. In this study, DIXD time resolution is acquired using a fiber bundle comprising 30 fibers of different lengths. Time resolution is obtained from the fiber-gating image in a single shot. In our method, the measurement error caused by shot-to-shot timing jitter can be avoided.

This study is an extension of our previous study [27]. An earlier study described a dilation UV imager with time-resolution measurements. The PC was developed on a fused silica window in a UV camera. The fused silica window blocked X-ray transmission to the PC so that the camera could not be used for X-ray measurements in the ICF. It was used for dilation performance testing with a UV laser in the laboratory. In this study, the DIXD is improved from a UV camera, and a gold PC is coated onto a C_8H_8 film to achieve an X-ray PC. Furthermore, while previous studies investigated the performance of the camera with a focus on improving its performance, this study focuses on the oscillographic application of the DIXD.

II. DETECTOR DESCRIPTION AND OSCILLOGRAPHIC PRINCIPLE

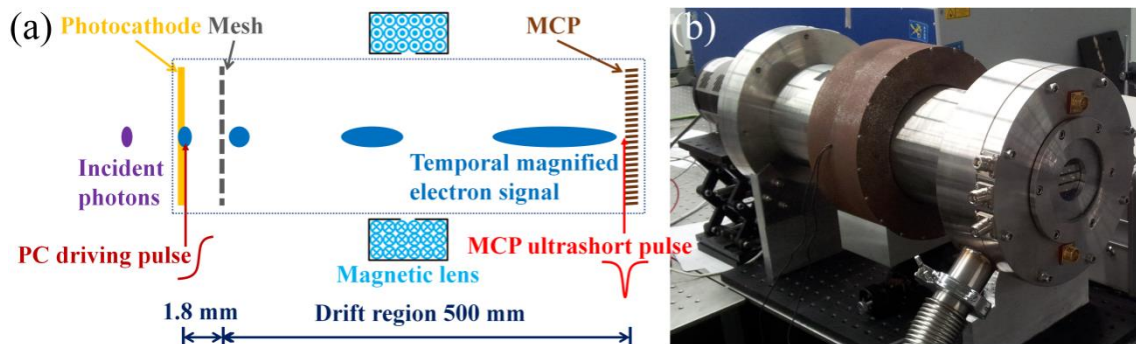


Fig. 1. (a) DIXD diagram. (b) DIXD photograph.

The DIXD comprises a temporally magnified electron pulse device, a sampling MCP imager, a magnetic lens, and a fast pulse generator, as shown in Figure 1. The temporally magnified electron pulse device increases the time

duration of the photoelectron pulse emitted from the PC. The device consists of three transmission photocathodes, an anode mesh, and a drift tube. The photocathodes are prepared by depositing 80 nm Au on a C_8H_8 film with a 56 mm diameter. Each PC has a microstrip transmission line structure and a width of 8 mm, and a 2.8 mm gap is left between PCs. A nickel mesh with a 10 lp/mm spatial frequency and 56 mm diameter is placed 1.8 mm from the PC. The mesh is parallel to the PC and the ground potential. The PC is applied with a driving pulse and biased by a negative DC high voltage, which produces a varied electric field to achieve electron energy dispersion. The electrons then enter the drift tube between the mesh and MCP. The 50 cm drift tube produces a temporal magnification of the electron pulse because of the higher flight speed of the front electrons. However, the electron pulse is spatially dispersed while it moves through the drift tube. To obtain sufficient spatial resolution, a magnetic lens is used to image the electron pulse from the PC to the MCP. An annular magnetic lens composed of a soft iron shield and 1200-turn copper coils is placed in the middle of the PC and MCP. The axial length, inner diameter, and outer diameter are 100 mm, 160 mm, and 256 mm, respectively. A circular slit with a width of 4 mm in the inner circumference is used for the magnetic field leaking from the soft iron to the drift tube to image the electron pulse. When the coil current is 0.34 A, the magnetic field images electrons with an energy of 3 keV on the MCP clearly with a 1:1 image ratio. Subsequently, the MCP imager with 78 ps time resolution samples the magnified electron pulse. The sampling MCP imager consists of an MCP signal sampling part, phosphor screen, and charge-coupled device (CCD). The MCP input surface is deposited on three microstrip lines formed by a Cu layer overlying the Au layer. Au and Cu films are also coated on the MCP output surface, which is successively deposited on the entire surface and connected to the ground. An ultrashort pulse is transmitted from one side of the MCP microstrip line to the other side. While the magnified electron pulse is synchronized with the ultrashort pulse, the electron pulse is sampled and amplified by the MCP. The electric field from the phosphor to the MCP accelerates the amplified electrons, and then the high-speed electrons impact the P20 phosphor, generating fluorescence. A CCD is used to collect the fluorescence. The MCP has a diameter of 56 mm, thickness of 0.5 mm, channel diameter of 12 μm , and bias angle of 6°. Each MCP microstrip line has an 8 mm width, and a 2.8 mm gap to the adjacent line. The phosphor is applied with a +4 kV DC high voltage and is placed 0.5 mm to the MCP.

The fast pulse generator generates both the PC driving pulse and the MCP ultrashort pulse, and the generator comprises an avalanche transistor circuit and a diode shaper. First, avalanche transistor stacks are formed in a Marx bank circuit to produce six fast step pulses. Three of these are employed to excite photocathodes, and an avalanche diode separately shapes the other three to acquire three MCP ultrashort pulses [28]. Each PC driving pulse has a maximum slope of approximately 1.6 V/ps. MCP ultrashort pulses are achieved with a width of 220 ps and an amplitude of -1.8 kV.

The time resolution is mainly dependent on the PC driving pulse slope, PC voltage, drift tube, and time resolution of the MCP signal sampling part [20]. In DIXD, the drift tube and MCP signal sampling part have invariant parameters. Therefore, the PC voltage and driving pulse slope determine time resolution. The PC voltage and driving pulse slope can also be obtained from the time-resolution results. In other words, the waveform of the PC driving pulse can be reconstructed from the DIXD time resolution, which shows that the DIXD can be used as an oscilloscope.

The time resolution T of the DIXD can be given by [29]

$$T = \sqrt{T_{phys}^2 + T_{tech}^2}, \quad (1)$$

where T_{phys} is the physical time resolution or limiting time resolution, which mainly depends on the transit time dispersion in the PC to the anode mesh region [29]. T_{tech} is the technology time resolution related to the time resolution of the MCP signal sampling part T_{MCP} and the temporal magnification factor M .

$$T_{phys} \approx \frac{2.63\sqrt{\delta\epsilon}}{E}, \quad (2)$$

$$E = \frac{\phi(t)}{L_{pa}}, \quad (3)$$

$$\phi(t) = [-V_B - V_P(t)], \quad (4)$$

where $\delta\epsilon$, which is in eV, is the full width at half maximum (FWHM) of the energy distribution of the electrons emitted from the PC. The $\delta\epsilon$ of Au under 266 nm illumination is approximately 0.5 eV [29]. E is in kV/mm and is the electric field from the anode mesh to the PC. $\phi(t)$ is the potential difference between the PC and anode mesh, while the photoelectron is produced at time t . L_{pa} is the length of 1.8 mm from the PC to the anode mesh. $V_B < 0$ is the PC bias voltage, which is -3 kV. $V_P(t)$ is the PC driving pulse voltage at time t . In addition, T_{phys} provides time dispersion in ps:

$$T_{tech} \approx \frac{T_{MCP}}{M}. \quad (5)$$

Generally, the sampling MCP imager parameters are fixed; therefore, the time resolution of the MCP signal sampling part T_{MCP} is constant. The temporal magnification factor M is mainly dependent on the drift tube, PC voltage, and driving pulse slope. In the limit of a small accelerating gap from the PC to the anode mesh and neglecting the initial energy spread of the electrons emitted from the PC, the electron that enters the drift tube at time t_i reaches the MCP at the following time [19]:

$$t'_i = \frac{L}{\sqrt{2e\phi(t_i)/m}} + t_i, \quad (6)$$

where L is the drift tube length (50 cm). e and m are the electron charge and mass, respectively. The temporal magnification factor M between the two time steps is as follows [27]:

$$\begin{aligned} M(t_{i+1}, t_i) &= \frac{t'_{i+1} - t'_i}{t_{i+1} - t_i} = 1 + \frac{L}{\sqrt{2e/m}} \frac{\phi(t_{i+1})^{-1/2} - \phi(t_i)^{-1/2}}{t_{i+1} - t_i} \\ &\approx 1 + \frac{L}{\sqrt{2e/m}} [\phi(t)^{-1/2}]'. \end{aligned} \quad (7)$$

$V_P(t)$ and $V'_P(t)$ have the following relation:

$$V'_P(t_{i+1}, t_i) = \frac{V_P(t_{i+1}) - V_P(t_i)}{t_{i+1} - t_i} = \frac{V_P(t_{i+1}) - V_P(t_i)}{\Delta t}. \quad (8)$$

The DIXD time resolution T and time resolution of the MCP signal sampling part T_{MCP} can be experimentally measured. Then, there are only two unknowns, $V_P(t)$ and $V'_P(t)$ in Equations (1)–(8), and they have the relation shown in Equation (8). Therefore, $V_P(t)$ can be obtained from Equations (1)–(8). The variation in the PC driving pulse voltage with time t , which is the PC driving pulse waveform, can then be acquired.

III. EXPERIMENTAL MEASUREMENT

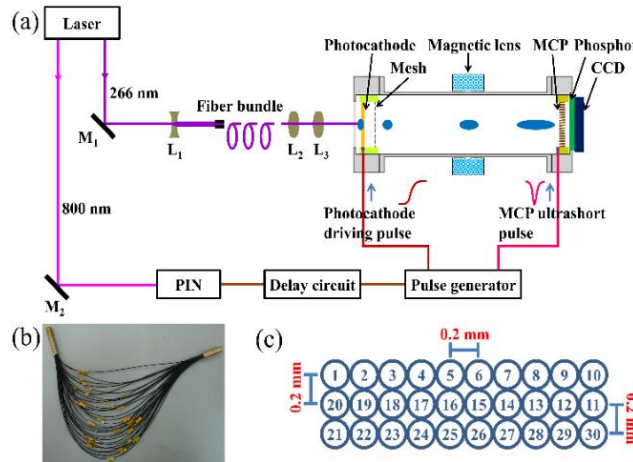


Fig. 2. (a) Schematic of the time resolution measurement setup. (b) The photograph of the fiber bundle. (c) The output port array of the fiber bundle. The fiber labeled number one has the shortest length, and the length is increased by 2 mm with each increase in 1. The gap between each two adjacent fibers is 0.2 mm.

The time resolution is measured using a Ti-sapphire laser system and a fiber bundle; the measurement setup is shown in Figure 2(a). The Ti-sapphire laser system outputs two laser beams: a 266 nm UV beam and 800 nm infrared light beam. The total reflection mirror M_1 first reflects the UV laser beam with a pulse width of 130 fs, and the light spot size is enlarged to be larger than the fiber bundle diameter using concave lens L_1 . The UV laser beam then reaches the fiber bundle, which consists of 30 fibers with equal differences in length. A photograph of the fiber bundle and schematic of the fiber array are shown in Figures 2(b) and 2(c), respectively. The fiber length is increased by a 2 mm step with an error of less than 0.2 mm. Then, 30 UV laser pulses are achieved and exported from the fiber bundle at various times. The delay time between each pair of adjacent fibers is 10 ps. Lenses L_2 and L_3 image the UV laser pulses on the PC to generate 30 photoelectron pulses. The infrared laser beam is reflected from total reflector M_2 to a positive-intrinsic-negative (PIN) diode to produce an electric signal, which triggers the fast pulse generator to produce the driving pulse on the PC and ultrashort pulse on the MCP. To ensure that the 266 nm laser pulses are synchronized with the PC driving pulse, a delay circuit is utilized to precisely adjust the trigger time. Then, the 30 photoelectron pulses with different emission times are accelerated by a varied electric field, which achieves electron velocity dispersion to magnify the time duration of the electron signal. Finally, the ultrashort pulse is timed to sample the magnified electron pulse on the MCP, and a gating image with time dilation is obtained.

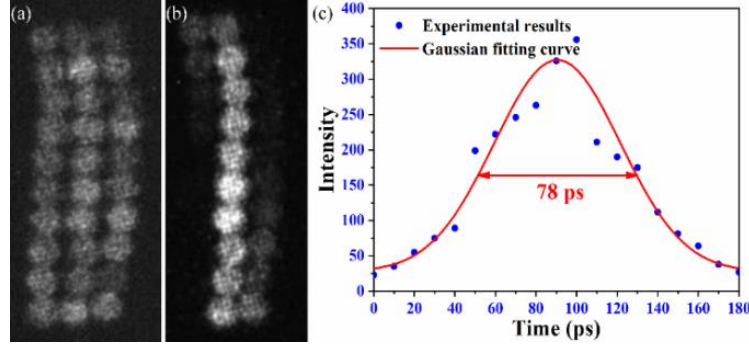


Fig. 3. (a) Static image of the 30 laser pulses, while the PC is subjected to a static DC bias of -3 kV and the MCP is subjected to a static DC bias of -700 V. (b) Gating image without time-dilation, a -3 kV DC bias is applied to the PC, and an ultrashort pulse plus a -300 V DC bias are applied on MCP. The ultrashort pulse has a width of 220 ps and an amplitude of -1.8 kV (c) Line out of the gating image without time-dilation in (b).

First, the time resolution of the MCP signal-sampling part T_{MCP} is measured. The measured static image of the 30 laser pulses and gating image without time dilation are shown in Figures 3(a) and 3(b), respectively. A -3 kV static DC bias is used for the PC and a -700 V for the MCP. A static image is obtained, as shown in Figure 3(a). The shortest fiber is imaged at the top right, and every two adjacent images are distanced by 0.5 mm. Figure 3(b) shows the gating image without time dilation, which was obtained by applying a -3 kV DC bias to the PC and an ultrashort pulse plus a -300 V DC bias to the MCP. The images in Figures 3(a) and 3(b) are raw. To avoid the influence of an uneven light intensity distribution, the experimental results in Figure 3(b) were calibrated using the static results in Figure 3(a). The line outside the calibrated results in Figure 3(b) is shown in Figure 3(c). The solid points are the calibrated experimental results, which were fitted using Gauss. The Gaussian curve is the intensity versus time curve, and its FWHM is defined as the time resolution. While the electron signal is not dilated, it can be seen from Figure 3(c) that the time resolution is approximately 78 ps, which is the time resolution of the MCP signal sampling part, T_{MCP} .

Then, the time resolution T , which varies with the synchronization position, is obtained. As the time the laser pulse takes to reach the PC is constant, changing and accurately adjusting the delay circuit in order to synchronize the UV laser pulse with the rising edge of the PC driving pulse is recommended. A schematic of the synchronization position for the laser pulse with the PC driving pulse is shown in Figure 4. Point t_1 was delayed by approximately 200 ps relative to the starting time of the PC driving pulse. The time was increased by 62.5 ps, while the subscript number was added by one until t_{11} . In other words, point t_2 was approximately 262.5 ps later than the PC driving pulse at the very beginning, point t_3 was approximately 325 ps, and point t_{11} was approximately 825 ps. Point t_{12} occurred approximately 1200 ps later than that at the beginning. The measured gating image when the synchronization position is point t_1 and the electron signal is dilated is shown in Figure 5(a). To obtain the gating image with time dilation, the MCP voltages used to obtain Figure 3(b) are retained, while a -3 kV DC bias overlapped by a driving pulse are applied to the PC. The line outside of the measurement results in Figure 5(a) is shown in Figure 6. Figure 6 shows that the DIXD time resolution T is approximately 39 ps with time dilation, whereas the synchronization position is point t_1 .

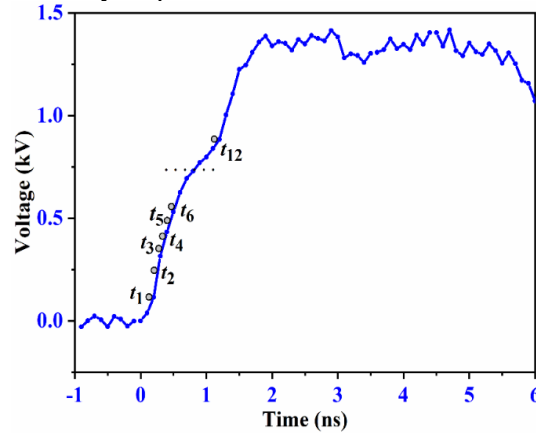


Fig. 4. Schematic of the synchronization position for the laser pulse with the driving pulse rising edge on the PC. The synchronization position is adjusted at points t_1 to t_{12} in turn.

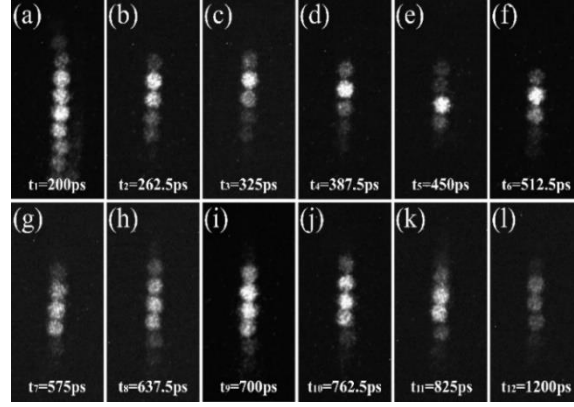


Fig. 5. Gating images with time-dilation while the synchronization position of the laser pulse and PC driving pulse is changed from point t_1 to t_{12} . A -3 kV DC bias overlapped by a driving pulse are applied on the PC, and the voltages applied to the MCP are a -300 V DC bias plus the ultrashort pulse. The gating images (a)–(l) correspond to the synchronization points t_1 – t_{12} .

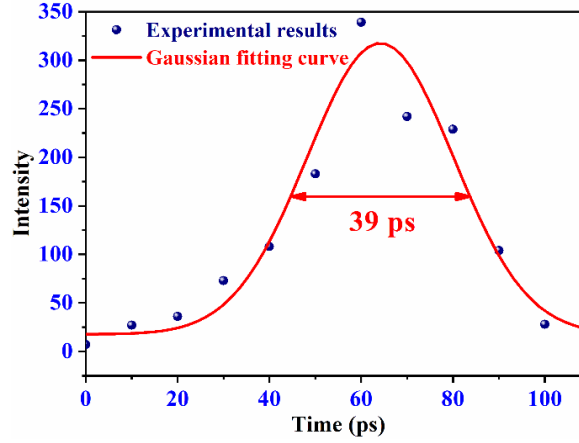


Fig. 6. Signaling out of the gating image with time-dilation in Fig. 5(a), while the synchronization position for laser pulse and PC driving pulse is point t_1 , 200 ps later than the very beginning.

To adjust the synchronization position to point t_2 , the delay time of the PC driving pulse was changed, and the gating image with time dilation for t_2 is shown in Figure 5(b). The synchronization position was adjusted at points t_3 to t_{12} in turn, and the gating image for each synchronization point was obtained successively, as shown in Figures 5(c)–5(l). The variation in the time resolution T with the synchronization position was then obtained from Figures 5(a)–5(l), as shown in Figure 7. The time resolution differs when the synchronization position is changed. The best time resolution was 12 ps, while the best synchronization position was t_5 , which was 450 ps later than that at the beginning.

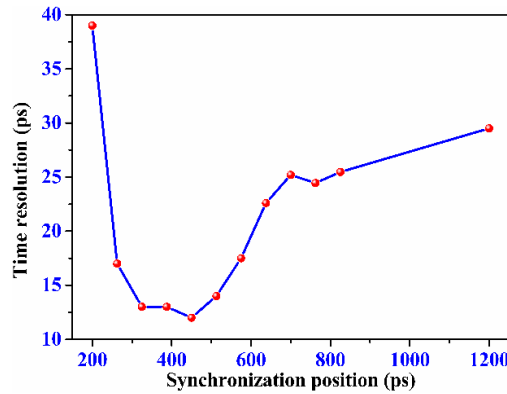


Fig. 7. DIXD time resolution T varying with the synchronization position.

In the DIXD, the magnetic lens images the photoelectrons from the PC to the MCP. A corresponding magnetic lens coil current needs to be used to make a certain energy photoelectron image clearly in the MCP, i.e., when the electron energy changes, the magnetic lens coil current changes accordingly. Therefore, we can use the coil current to obtain the electron energy to determine the potential difference between the PC and anode mesh. While the synchronization position of the PC driving pulse is located at point t_1 , the coil current should be 0.33 A to obtain the clear spot image shown in Figure 5(a). An experiment was performed to obtain the photoelectron energy related to the 0.33 A coil current. Only the PC voltage was changed, and the other conditions, such as the coil current and MCP voltage, remained the same as in Figure 5(a). A DC bias with no PC driving pulse was applied to the PC. The PC DC bias was adjusted precisely to obtain the gating image, which was decoupled from time dilation. While the PC DC bias was approximately -2.88 kV, the gating image without time-dilation was as clear as the spot image in Figure 5(a). Therefore, the 0.33 A coil current corresponds to a photoelectron energy of 2.88 keV. In Figure 5(a), PC is applied with a -3 kV DC bias overlaid by a driving pulse, and the photoelectron energy is 2.88 keV. Therefore, the PC driving pulse is approximately 120 V at synchronization point t_1 . In Equations (1)–(8), the acquired parameters at synchronization point t_1 are $T(t_1) = 39$ ps, $T_{MCP} = 78$ ps, and $V_p(t_1) = 120$ V. Then, $V'_p(t)$ can be calculated from Equations (1)–(8). A value of 0.37 V/ps was obtained. The parameters for point t_2 are $V_p(t_2) = 199$ V, $T(t_2) = 17$ ps, and $T_{MCP} = 78$ ps, and the values of $V_p(t_2)$ and $V'_p(t_2)$ are 199 V and 1.26 V/ps, respectively, as calculated from Equations (1)–(8). Subsequently, the variations in $V_p(t)$ and $V'_p(t)$ with time t can be acquired, as shown in Table 1.

The waveform of the PC driving pulse from points t_1 to t_{12} measured by the DIXD can be obtained from Table 1, and is represented by the red part in Figure 8. The blue part of Figure 8 shows the PC driving pulse waveform measured using a high-speed oscilloscope. Figure 8 shows that the waveforms from points t_1 to t_{12} measured by the DIXD and oscilloscope are almost the same, and the difference between them is within 6%, which validates the oscilloscopic capability of the DIXD.

Table 1. $V_p(t)$ and $V'_p(t)$ vary with the synchronization position, which is the point at the rising edge of the PC driving pulse t ps later than that at the beginning.

Point	t_1	t_2	t_3	t_4	t_5	t_6	t_7	t_8	t_9	t_{10}	t_{11}	t_{12}
t (ps)	200	262.5	325	387.5	450	512.5	575	637.5	700	762.5	825	1200
$V_p(t)$ (V)	120	199	303	402	504	585	644	685	719	754	786	925
$V'_p(t)$ (V/ps)	0.37	1.26	1.66	1.58	1.63	1.3	0.94	0.66	0.54	0.56	0.51	0.37

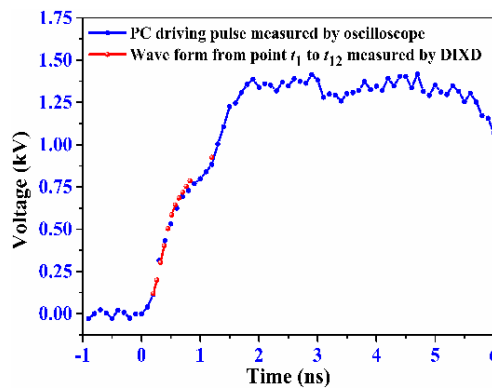


Fig. 8. PC driving pulse waveform measured by a high-speed oscilloscope, and the waveform from point t_1 to t_{12} was measured by the DIXD.

The limiting time resolution of the DIXD is considered equal to the physical time resolution T_{phys} [30]. The red curve in Figure 9 shows the variation in the limiting time resolution with the potential difference between the PC and mesh, whereas the space between the grounded anode mesh and PC is 1.8 mm. The larger the potential difference, the smaller the transit time dispersion of the electron in the PC to the mesh region and the higher the limiting time

resolution. When the DIXD is used as an oscilloscope, the relationship between its maximum theoretical bandwidth and the potential difference is shown by the blue curve in Figure 9. The bandwidth is limited by the potential difference. When the potential difference is 3.4 kV, the theoretical limiting bandwidth is 1000 GHz. Furthermore, the bandwidth increases with increasing potential difference.

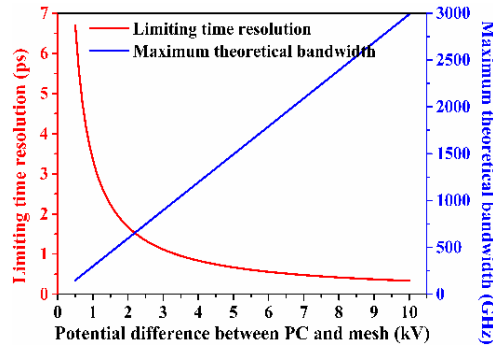


Fig. 9. Limiting time resolution and maximum theoretical bandwidth of the DIXD oscilloscope vary with the potential difference between the PC and mesh.

IV. CONCLUSIONS

A DIXD composed of a temporally magnified electron pulse device, a sampling MCP imager, a magnetic lens, and a fast pulse generator is developed. The temporally magnified device achieves a dilation electron signal, and the DIXD time resolution is improved from 78 ps to 12 ps. A DIXD oscilloscope is presented and theoretically analyzed. Typically, the time resolution depends on factors such as the PC voltage, PC driving pulse slope, time resolution of the MCP signal sampling part, and drift tube length. In the DIXD, the time resolution of the MCP signal sampling part is 78 ps, and the drift tube is 50 cm, which were invariant. Therefore, the slope and voltage of the PC driving pulse determine the time resolution, and they can be obtained from the time resolution. The PC driving pulse waveform can then be presented based on the DIXD time resolution. In other words, the DIXD can be used as an oscilloscope. An experiment is conducted to establish an oscillographic application of the DIXD. The synchronization position for the laser pulse with the PC driving pulse is adjusted at different points, and the time resolution T at each synchronization position can be obtained. Then, the waveform for the PC driving pulse appears after the pulse voltage and slope at each synchronization position are obtained from the measured time resolution. The waveform from point t_1 to t_{12} is measured using DIXD and a high-speed oscilloscope. The two waveforms are almost identical, and the difference between them is within 6%. The maximum theoretical bandwidth of the DIXD oscilloscope varies with the potential difference between the mesh and the PC. The bandwidth is limited by the potential difference. When the potential difference is 3.4 kV, the theoretical limiting bandwidth is 1000 GHz. The larger the potential difference, the higher the bandwidth. Therefore, the bandwidth of the DIXD oscilloscope can be improved by increasing the potential difference. This study provides a novel approach for the development of new high-speed oscilloscopes.

-
- [1] V. Gopalaswamy, R. Betti, J. P. Knauer et al., Tripled yield in direct-drive laser fusion through statistical modelling. *Nature* **565**, 581–586 (2019). doi: 10.1038/s41586-019-0877-0
 - [2] G. N. Hall, C. M. Krauland, M. S. Schollmeier et al., The Crystal Backlighter Imager: A spherically bent crystal imager for radiography on the National Ignition Facility. *Rev. Sci. Instrum.* **90**, 013702 (2019). doi: 10.1063/1.5058700
 - [3] Q. Q. Wang, Z. R. Cao, T. Chen et al., Theoretical study on temporal and spatial performance of magnetic solenoid used in dilation x-ray imager. *Rev. Sci. Instrum.* **91**, 073302 (2020). doi: 10.1063/1.5133395
 - [4] E. Aboud, S. Ahn, G. V. Rogachev et al., Modular next generation fast-neutron detector for portal monitoring. *Nucl. Sci. Tech.* **33**, 13 (2022). doi: 10.1007/s41365-022-00990-7.
 - [5] L. Yang, H. R. Cao, J. L. Zhao et al., Development of a wide-range and fast-response digitizing pulse signal acquisition and processing system for neutron flux monitoring on EAST. *Nucl. Sci. Tech.* **33**, 35 (2022). doi: 10.1007/s41365-022-01016-y.
 - [6] Z. Yuan, T. Chen, Z. W. Yang et al., Method to measure the temporal resolution of x-ray framing camera. *Opt. Eng.* **57**, 074101 (2018). doi: 10.1117/1.OE.57.7.074101
 - [7] P. Hu, Z. G. Ma, K. Zhao et al., Development of gated fiber detectors for laser-induced strong electromagnetic pulse environments. *Nucl. Sci. Tech.* **32**, 58 (2021). doi: 10.1007/s41365-021-00898-8.

- [8] G. L. Gao, K. He, J. S. Tian et al., Ultrafast all-optical solid-state framing camera with picosecond temporal resolution. *Opt. Express* **25**, 8721–8729 (2017). doi: 10.1364/OE.25.008721
- [9] J. H. Liu, Z. Ge, Q. Wang et al., Electrostatic-lenses position-sensitive TOF MCP detector for beam diagnostics and new scheme for mass measurements at HIAF. *Nucl. Sci. Tech.* **30**, 152 (2019). doi: 10.1007/s41365-019-0676-1.
- [10] J. A. Frenje, Nuclear diagnostics for Inertial Confinement Fusion (ICF) plasmas. *Plasma Phys. Contr. F* **62**, 023001 (2020). doi: 10.1088/1361-6587/ab5137
- [11] S. E. Jiang, F. Wang, Y. K. Ding et al., Experimental progress of inertial confinement fusion based at the ShenGuang-III laser facility in China. *Nucl. Fusion*. **59**, 032006 (2019). doi: 10.1088/1741-4326/aabdb6
- [12] S. R. Nagel, A. C. Carpenter, J. Park et al., The dilation aided single-line-of-sight x-ray camera for the National Ignition Facility: Characterization and fielding. *Rev. Sci. Instrum.* **89**, 10G125 (2018). doi: 10.1063/1.5038671
- [13] W. Theobald, C. Sorce, M. Bedzyk et al., The single-line-of-sight, time-resolved x-ray imager diagnostic on OMEGA. *Rev. Sci. Instrum.* **89**, 10G117 (2018). doi: 10.1063/1.5036767
- [14] J. D. Kilkenny, High speed proximity focused X-ray cameras. *Laser Part. Beams*. **9**, 49–69 (1991). doi: 10.1017/S0263034600002330
- [15] P. M. Bell, J. D. Kilkenny, R. L. Hanks et al., Measurements with a 35 psec gate time microchannel plate camera. *Proc. SPIE*. **1346**, 456–464 (1991). doi: 10.1117/12.23371
- [16] S. R. Nagel, L. R. Benedetti, D. K. Bradley et al., Comparison of implosion core metrics: A 10 ps dilation X-ray imager vs a 100 ps gated microchannel plate. *Rev. Sci. Instrum.* **87**, 11E311 (2016). doi: 10.1063/1.4959917
- [17] K. Engelhorn, T. J. Hilsabeck, J. Kilkenny et al., Sub-nanosecond single line-of-sight (SLOS) x-ray imagers. *Rev. Sci. Instrum.* **89**, 10G123 (2018). doi: 10.1063/1.5039648
- [18] T. J. Hilsabeck, J. D. Hares, J. D. Kilkenny et al., Pulse-dilation enhanced gated optical imager with 5 ps resolution. *Rev. Sci. Instrum.* **81**, 10E317 (2010). doi: 10.1063/1.3479111
- [19] S. R. Nagel, T. J. Hilsabeck, P. M. Bell et al., Investigating high speed phenomena in laser plasma interactions using dilation x-ray imager. *Rev. Sci. Instrum.* **85**, 11E504 (2014). doi: 10.1063/1.4890396
- [20] S. R. Nagel, T. J. Hilsabeck, P. M. Bell et al., Dilation x-ray imager a new/faster gated x-ray imager for the NIF. *Rev. Sci. Instrum.* **83**, 10E116 (2012). doi: 10.1063/1.4732849
- [21] R. D. Prosser, Electron-dispersion technique for observation of fast transient signals. *J. Phys. E: Sci. Instrum.* **9**, 57–59 (1976). doi: 10.1088/0022-3735/9/1/018
- [22] H. Geppert-Kleinrath, H. W. Herrmann, Y. H. Kim et al., Pulse dilation gas Cherenkov detector for ultra-fast gamma reaction history at the NIF. *Rev. Sci. Instrum.* **89**, 10I146 (2018). doi: 10.1063/1.5039377
- [23] S. G. Gales, C. J. Horsfield, A. L. Meadowcroft et al., Characterisation of a sub-20 ps temporal resolution pulse dilation photomultiplier tube. *Rev. Sci. Instrum.* **89**, 063506 (2018). doi: 10.1063/1.5031110
- [24] J. Feng, K. Engelhorn, B. I. Cho et al., A grazing incidence x-ray streak camera for ultrafast, single-shot measurements. *Appl. Phys. Lett.* **96**, 134102 (2010). doi: 10.1063/1.3371810
- [25] I. Konvalina and I. Müllerová, Properties of the cathode lens combined with a focusing magnetic/immersion-magnetic lens. *Nucl. Instrum. Meth. A* **645**, 55–59 (2011). doi: 10.1016/j.nima.2010.12.232
- [26] Z. Chang, A. Rundquist, J. Zhou et al., Demonstration of a sub-picosecond x-ray streak camera. *Appl. Phys. Lett.* **69**, 133–135 (1996). doi: 10.1063/1.118099
- [27] H. Z. Cai, X. Zhao, J. Y. Liu et al., Dilation framing camera with 4 ps resolution. *APL Photonics* **1**, 016101 (2016). doi: 10.1063/1.4945350
- [28] P. M. Bell, J. D. Kilkenny, O. L. Landen et al., Electrical characteristics of short pulse gated microchannel plate detectors. *Rev. Sci. Instrum.* **63**, 5072–5074 (1992). doi: 10.1063/1.1143495
- [29] M. M. Shakya and Z. H. Chang, Achieving 280 fs resolution with a streak camera by reducing the deflection dispersion. *Appl. Phys. Lett.* **87**, 041103 (2005). doi: 10.1063/1.2001732
- [30] D. Cesar and P. Musumeci, Temporal magnification for streaked ultrafast electron diffraction and microscopy. *Ultramicroscopy* **199**, 1–6 (2019). doi: 10.1016/j.ultramic.2019.01.003